INTERNATIONAL JOURNAL FOR NUMERICAL METHODS IN FLUIDS, VOL. 11, 427–444 (1990)

FOURIER ANALYSIS OF THE EULERIAN–LAGRANGIAN LEAST SQUARES COLLOCATION METHOD

L. R. BENTLEY AND A. ALDAMA

Department of Civil Engineering and Operations Research, Princeton University, Princeton, NJ 08544, U.S.A.

AND

G. F. PINDER

College of Engineering and Mathematics, University of Vermont, Burlington, VT 05405, U.S.A.

SUMMARY

A Fourier analysis was performed in order to study the numerical characteristics of the effective Eulerian–Lagrangian least squares collocation (ELLESCO) method. As applied to the transport equation, ELLESCO requires a C^1-continuous trial space and has two degrees of freedom per node. Two coupled discrete equations are generated for a typical interior node for a one-dimensional problem. Each degree of freedom is expanded separately in a Fourier series and is substituted into the discrete equations to form a homogeneous matrix equation. The required singularity of the system matrix leads to a 'physical' amplification factor that characterizes the numerical propagation of the initial conditions and a 'computational' one that can affect stability.

Unconditional stability for time-stepping weights greater than or equal to 0·5 is demonstrated. With advection only, ELLESCO accurately propagates spatial wavelengths down to $2\Delta x$. As the dimensionless dispersion number becomes large, implicit formulations accurately propagate the phase, but the higher-wave-number components are underdamped. At large dispersion numbers, phase errors combined with underdamping cause oscillations in Crank–Nicolson solutions. These effects lead to limits on the temporal discretization when dispersion is present. Increases in the number of collocation points per element improve the spectral behaviour of ELLESCO.

KEY WORDS Fourier analysis Eulerian–Lagrangian Least squares Transport

INTRODUCTION

Classical finite element and finite difference solutions to the advective–dispersive transport equation are contaminated by serious phase and amplitude errors when the advection term becomes large.[1] Methods known as 'Eulerian–Lagrangian methods' (ELMs) or the 'Modified method of characteristics' (MMOC) have been developed to improve the behaviour of numerical solutions when advection dominates.[2–12] This class of methods solves the transport equation in two steps. The first step tracks back or projects forward one time level along the characteristics of the first-order terms of the transport equation and hence is Lagrangian in nature. Using the information derived from the first step, in the second step one solves the resultant equations on a fixed, or Eulerian, spatial grid. The Lagrangian step of ELMs eliminates the troublesome first-order terms from the algebraic system of equations, and deforming grids associated with purely Lagrangian schemes are avoided. Recently, Bentley *et al.*[13] introduced the 'Eulerian–Lagrangian

0271–2091/90/120427–18$09.00
© 1990 by John Wiley & Sons, Ltd.
Received 22 August 1989
Revised 19 January 1990

least squares collocation' (ELLESCO) method. In ELLESCO one approximates the time derivative as a finite difference along the characteristics of the first-order terms of the equation. The spatial portion of the equation is discretized using cubic Hermite basis functions in conjunction with a least squares collocation metod of weighted residuals. Comparison of ELLESCO test problem results with the results of other ELMs and the Galerkin finite element method demonstrated the enhanced accuracy of the method. Because of these encouraging results, a Fourier analysis of the procedure is presented in this paper.

Fourier analysis is a well known tool for studying the behaviour of discretized systems. Although Fourier analysis is limited to regular grids with constant coefficients and does not account for boundary conditions, it yields results that describe the local nature of the solution propagation and its stabilitiy.

As discussed by Bentley *et al.*,[13] ELLESCO requires continuity of the function and the first spatial derivative at the element boundaries. Cubic Hermite basis functions are used to satisfy this requirement, and there are two basis functions associated with each node. We approach the Fourier analysis of ELLESCO in a manner similar to the development of the Fourier analysis for linearized forms of the coupled shallow water equations.[1] Accordingly, we derive a set of two coupled homogeneous equations that is associated with a typical interior node. The two degrees of freedom associated with each node are expanded separately in Fourier series, and the Fourier series expansions are substituted into the discrete equations to form a homogeneous matrix equation. For non-trivial solutions to exist, the determinant of the coefficient matrix of this system must equal zero. This condition will lead to a quadratic equation that can be solved for the 'physical root' of an amplification factor that characterizes the propagation of a Fourier mode of the initial condition and another 'computational' root that can affect the stability. The amplification factors are used to demonstrate the stability and accuracy of the ELLESCO method.

DISCRETE EQUATIONS

In this section we derive the set of two discrete equations which represents the ELLESCO equations at any node away from the domain boundaries. The equations are used in the next section for the Fourier analysis derivation. A thorough development of the ELLESCO equations for the generalized one-dimensional parabolic partial differential equation can be found in Reference 13 and will not be repeated here. Instead, we will summarize the development for the one-dimensional advective–dispersive transport equation with constant coefficients, because it is the equation used in this paper for the Fourier analysis:

$$\frac{\partial C}{\partial t} + V\frac{\partial C}{\partial x} - \mathrm{D}\frac{\partial^2 C}{\partial x^2} = 0, \tag{1}$$

where C is the concentration, V is the flow velocity and D is the dispersion coefficient. Equation (1) can also be written in Lagrangian co-ordinates as

$$\left(\frac{\partial C}{\partial t}\right)_{\chi} - \mathrm{D}\frac{\partial^2 C}{\partial \chi^2} = 0, \tag{2}$$

where $\chi = x - Vt$ is a co-ordinate system that follows the fluid motion.

Equation (2) is now discretized using finite differences in time and finite elements in space. Temporal indices are denoted by n such that $t = n\Delta t$. Spatial indices are denoted by p such that node locations are $x = p\Delta x$ (Figure 1). ELLESCO requires the evaluation of residuals at discrete points referred to as collocation points. The number of collocation points per element will be

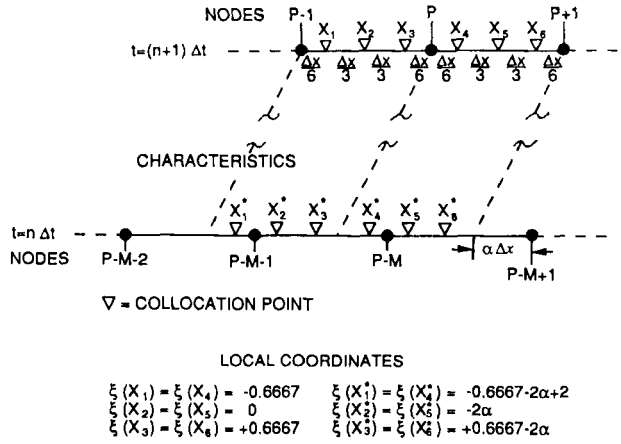

Figure 1. Discretization geometry. The discretization at a typical interior node P with a three-collocation-point pattern is shown. Identical spatial grids are used at time levels n and $n+1$; however, different portions of the grid contribute to the equations associated with node P. The $n+1$ time level collocation points are spread over two elements, but their back-tracked locations are spread over three elements. The elemental co-ordinates of the back-tracked collocation points x_i^* are functions of α. The contributing nodes at the n time level are determined by M

characterized by the parameter *ncel*, and the number and location of the collocation points are assumed the same for all elements. Collocation points are separated by $\Delta x/ncel$. Figure 1 contains the collocation point pattern for the $ncel = 3$ case.

We now write the finite difference approximation to equation (2) for a collocation point x_k in terms of the Eulerian co-ordinate system (x, t):

$$C(x_k, t_{n+1}) - C(x_k^*, t_n) - \Delta t \Theta D \frac{\partial^2 C(x_k, t_{n+1})}{\partial x^2} - \Delta t(1-\Theta) D \frac{\partial^2 C(x_k^*, t_n)}{\partial x^2} = 0, \tag{3}$$

where $0 \leqslant \Theta \leqslant 1$ is a time-stepping weight and $x_k^* = x_k - V\Delta t$. The position x_k of a collocation point at time level $n+1$ can be projected back along the flow line passing through it to x_k^* at time level n. As an example, consider the collocation point x_1 in Figure 1.The first and third terms of equation (3) are evaluated at x_1, and the second and fourth terms are evaluated at the back-tracked location x_1^*.

Owing to the second-order spatial derivatives and the use of the least squares procedure, we require trial functions that are continuous in the value of the function and the first derivative at all points in the domain, including element boundaries. A trial function constructed with cubic Hermite polynomials will satisfy these conditions, and Figure 2 shows the notation, algebraic form and graphical illustration of the cubic Hermite basis. As usual, we have defined the basis functions in terms of the local or elemental co-ordinate system $-1 \leqslant \xi \leqslant 1$. The cardinal basis functions associated with each node are constructed from the functions defined in Figure 2:

$$\Phi_p^0(x) = \begin{cases} \Phi_1^0(\xi(x)), & (p-1)\Delta x \leqslant x \leqslant p\Delta x, \\ \Phi_0^0(\xi(x)), & p\Delta x \leqslant x \leqslant (p+1)\Delta x, \end{cases} \tag{4a}$$

$$\Phi_p^1(x) = \begin{cases} \Phi_1^1(\xi(x)), & (p-1)\Delta x \leqslant x \leqslant p\Delta x, \\ \Phi_0^1(\xi(x)), & p\Delta x \leqslant x \leqslant (p+1)\Delta x, \end{cases} \tag{4b}$$

and zero elsewhere.

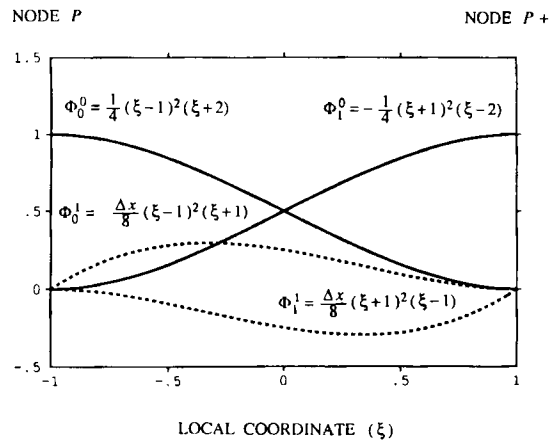

Figure 2. Cubic Hermite basis functions. Two cubic Hermite basis functions are associated with each node, and four functions contribute to interpolations within an element. Basis functions are defined on an elemental co-ordinate system. Local co-ordinates are related to global co-ordinates by the expression $\xi = 2(x/\Delta x - P) - 1$

The trial function at time level n is

$$\hat{C}^n = \sum_{p=1}^{P} [C_p^n \Phi_p^0(x) + CX_p^n \Phi_p^1(x)], \tag{5}$$

where P is the total number of nodes and the coefficients C_p^n and CX_p^n are the values of the trail function and the derivative of the trial function respectively at node p and time level n. Of course, in the interior of the elements the value of the function and the derivative are computed using a linear combination of the four basis functions associated with the element.

The ELLESCO system of algebraic equations is arrived at as follows. The residual R_k is formed by substituting the trial function, equation (5), into equation (3) and evaluating the result at each collocation point k. The sum of the squares of the residuals is then obtained and is minimized by taking the derivatives with respect to each of the unknown coefficients and setting the derivatives equal to zero. Two equations are generated at each node, one from the derivative with respect to C_p^{n+1} and one from the derivative with respect to CX_p^{n+1}. If the domain contains $P+1$ nodes, a system of $2P+2$ equations is formed. Away from the boundaries the assumptions of constant coefficients, constant discretization intervals and an identical pattern of collocation point locations within each element imply that all nodes have identical sets of associated equations, which can be written for the node p as

$$\sum_{k \in K_p} R_k \frac{\partial R_k}{\partial C_p^{n+1}} = \sum_{k \in K_p} R_k \left(\Phi_{pk}^0 - \Delta t \Theta \mathrm{D} \frac{\partial^2 \Phi_{pk}^0}{\partial x^2} \right) = 0, \tag{6a}$$

$$\sum_{k \in K_p} R_k \frac{\partial R_k}{\partial CX_p^{n+1}} = \sum_{k \in K_p} R_k \left(\Phi_{pk}^1 - \Delta t \Theta \mathrm{D} \frac{\partial^2 \Phi_{pk}^1}{\partial x^2} \right) = 0, \tag{6b}$$

where

$$R_k = \sum_{q=p-1}^{p+1} (C_q^{n+1} \Phi_{qk}^0 + CX_q^{n+1} \Phi_{qk}^1) - \hat{C}_{k*}^n$$
$$- \Delta t \Theta \mathrm{D} \frac{\partial^2}{\partial x^2} \sum_{q=p-1}^{p+1} (C_q^{n+1} \Phi_{qk}^0 + CX_q^{n+1} \Phi_{qk}^1) - \Delta t (1-\Theta) \mathrm{D} \frac{\partial^2 \hat{C}_{k*}^n}{\partial x^2}. \tag{7}$$

The subscript k indicates that the basis function is evaluated at the location x_k, and $\hat{C}^n_{k*}$ denotes $\hat{C}(x^*_k, t_n)$. The notation $k \in K_p$ indicates the collocation points contained in the region of support of the basis functions of node p or, in other words, the collocation points that fall in the two elements which are adjacent to node p. For the example in Figure 1 the summation is over points x_1 to x_6. The large parentheses of equation (6) contain the derivatives of the residuals with respect to the appropriate unknown coefficients. The difference between equations (6a) and (6b) is simply the difference between the right-hand portion of the products or, in method of weighted residuals terminology, the difference between the weighting functions.

The dimensionless dispersion number $D \equiv D\Delta t/(\Delta x)^2$, the Courant number $Co \equiv V\Delta t/\Delta x = M + \alpha$ and the Peclet number $Pe \equiv Co/D$ are dimensionless parameters used to characterize the temporal and spatial discretization of the transport equation. The dispersion number is a measure of the amount of dispersion that occurs during a single time step, the Courant number is a measure of the distance that is travelled by the flow field in a time step and the Peclet number is a measure of the relative strength of advection and dispersion. The Courant number has been decomposed into an integer portion $M \geqslant 0$ and a fractional portion $0 \leqslant \alpha < 1$. The equations used for the Fourier analysis will include the dispersion number D, the integer Courant number M and the fractional Courant number α as dimensionless parameters.

We now summarize some algebraic manipulations that will not be duplicated here. After substituting equation (7) into (6) and rearranging, the cardinal basis functions are replaced by local basis equivalents, and the spatial derivatives $\partial^2(\cdot)/\partial x^2$ are replaced by their local co-ordinate equivalents $(4/\Delta x^2)\,\partial^2(\cdot)/\partial \xi^2$. The variable $\hat{C}^n_{k*}$ must be expanded in terms of the local basis and the known coefficients at time level n.

The location of x^*_k is strictly a function of x_k and the Courant number. Referring to Figure 1, we see that a collocation point is shifted back in space M full elements and α partial elements. In general, collocation points that are spread over the two elements of interest in the $n+1$ time level will end up spread over three elements in the n time level. Note that the local co-ordinate associated with x^*_k is dependent only on the fractional Courant number α and that the integer Courant number M determines which nodes are to be used in the evaluation of $\hat{C}^n_{k*}$ and its second derivative.

After performing the above manipulations and summing over the collocation points contained in the elements adjacent to node p, equation (6) becomes

$$\begin{aligned} &a^j_1 C^{n+1}_{p-1} + a^j_2 CX^{n+1}_{p-1} + a^j_3 C^{n+1}_p + a^j_4 CX^{n+1}_p + a^j_5 C^{n+1}_{p+1} + a^j_6 CX^{n+1}_{p+1} \\ &\quad -(f^j_1 C^n_{p-M-2} + f^j_2 CX^n_{p-M-2} + f^j_3 C^n_{p-M-1} + f^j_4 CX^n_{p-M-1} \\ &\quad + f^j_5 C^n_{p-M} + f^j_6 CX^n_{p-M} + f^j_7 C^n_{p-M+1} + f^j_8 CX^n_{p-M+1}) = 0, \quad j = 0, 1. \end{aligned} \tag{8}$$

A detailed evaluation of the coefficients of equation (8) for the example illustrated in Figure 1 is found in Appendix I. Coefficients a^j_1 to a^j_6 and f^j_1 to f^j_8 are functions of Θ, D and, through the number and implied locations of the collocation points, *ncel*. Coefficients f^j_1 to f^j_8 are also dependent on the fractional Courant number α.

The two discrete equations represented by equation (8) are in the form of difference equations which will be used for the Fourier analysis.

FOURIER ANALYSIS OF ELLESCO EQUATIONS

Fourier analysis is a well known technique for quantitatively investigating the propagation characteristics of the individual spatial frequencies of the solution to the transport equation. In this section we derive the complex amplification factors which characterize the numerical

propagation of each Fourier series component by the ELLESCO method. We also present the amplification factors of the analytical solution as a comparsion.

The analytical derivation has been presented in detail elsewhere[1, 14] and only a brief summary is presented here. The analytical solution of equation (1) is assumed to have the form

$$C(x, t) = \sum_{m=-\infty}^{m=\infty} \mathrm{F}_m \exp[\mathrm{i}(\beta_m t + \sigma_m x)], \tag{9}$$

where F_m are complex coefficients determined by the initial conditions, $\sigma_m = 2\pi/L_m$ are the wave numbers, L_m are the spatial wavelengths, β_m are the temporal frequencies and 'i' is the square root of minus one.

Equation (1) is linear, so we can analyse each Fourier component separately. Substitution of one component of the series represented by equation (9) into equation (1) leads to a relation between β_m and σ_m. We can use that relation to eliminate β_m from equation (9). A general term of equation (9) becomes

$$c_m = \mathrm{F}_m \exp(-\mathrm{D}\sigma_m^2 t) \exp[\mathrm{i}\sigma_m(x - Vt)]. \tag{10}$$

The amplitude of the mth component is determined by the first two factors on the right-hand side of equation (10) and the translation by the last. The amplification factor is that portion of equation (10) which determines how the solution evolves as time increases. Anticipating the form of the computed amplification factor, we introduce $t = n\Delta t$ into equation (10) and arrive at

$$c_m = \mathrm{F}_m \exp(\mathrm{i}\sigma_m x)\lambda_m^n, \tag{11}$$

where $\lambda_m = \exp[-(\mathrm{D}\sigma_m^2 + \mathrm{i}\sigma_m V)\Delta t]$ is the analytic amplification factor. It determines the amount of change in the amplitude and phase on the mth component over one time step interval.

We now turn to the analysis of the ELLESCO numerical method. The two degrees of freedom associated with each node behave as independent state variables and can be represented by separate discrete Fourier series. This is analogous to the treatment of velocity and wave height in the Fourier analysis of the linearized shallow water wave equations.[1] We assume that the two solutions can be expanded as

$$\begin{aligned} C_p^n &= \sum_{m=0}^{P-1} U_m \exp[\mathrm{i}(\beta_m n\Delta t + \sigma_m p\Delta x)], \\ CX_p^n &= \sum_{m=0}^{P-1} UX_m \exp[\mathrm{i}(\beta_m n\Delta t + \sigma_m p\Delta x)], \end{aligned} \tag{12}$$

where m is the wave number index and $P + 1$ is the total number of nodes. U_m and UX_m are determined from the initial conditions.

As is typicial we define the amplification factor of the numerical solution as

$$\tilde{\lambda}_m = \exp(\mathrm{i}\beta_m \Delta t). \tag{13}$$

We also introduce the dimensionless wavelength

$$\bar{L}_m = L_m/\Delta x \tag{14}$$

and the dimensionless wave number

$$\bar{\sigma}_m = \sigma_m \Delta x = 2\pi/\bar{L}_m. \tag{15}$$

The system we are analysing is linear, so we can treat the Fourier components individually. A single mode from equation (12) is substituted into equation (8) along with equations (13) and (15).

The subscript m is dropped and after simplifying we get

$$(a_1^j U + a_2^j UX)\tilde{\lambda}e^{-i\sigma} + (a_3^j U + a_4^j UX)\tilde{\lambda} + (a_5^j U + a_6^j UX)\tilde{\lambda}e^{i\sigma}$$
$$-e^{-i\sigma M}[(f_1^j U + f_2^j UX)\tilde{\lambda}e^{-i2\sigma} + (f_3^j U + f_4^j UX)\tilde{\lambda}e^{-i\sigma}$$
$$+ (f_5^j U + f_6^j UX)\tilde{\lambda} + (f_7^j U + f_8^j UX)\tilde{\lambda}e^{i\sigma}] = 0, \quad j = 0, 1. \tag{16}$$

We can also write equation (16) in matrix form as (see Appendix II)

$$\begin{pmatrix} \mu_{11} & \mu_{12} \\ \mu_{21} & \mu_{22} \end{pmatrix} \begin{pmatrix} U \\ UX \end{pmatrix} = 0. \tag{17}$$

For non-trivial solutions to exist, the determinant of the coefficient matrix of the above system must equal zero, or

$$\mu_{11}\mu_{22} - \mu_{12}\mu_{21} = 0. \tag{18}$$

Equation (18) is quadratic in $\tilde{\lambda}$ and we can apply the quadratic formula to obtain the complex amplification factor

$$\tilde{\lambda} = \tilde{\lambda}(D, \Theta, M, \alpha, ncel, \sigma) = \frac{e^{-i\sigma M}}{2\bar{a}}[-\bar{b} \pm \sqrt{(\bar{b}^2 - 4\bar{a}\bar{c})}]. \tag{19}$$

At this point we restrict ourselves to a summary of the main features of equation (19) and refer the reader to Appendix II for a more detailed description of the derivation and form of the terms. The coefficient $\bar{a}$ is real and a function of D, Θ, *ncel* and σ. In general, $\bar{b}$ and $\bar{c}$ are complex and functions of D, Θ, σ, *ncel* and α. The fractional Courant number influences both the phase and amplitude of the solution. The influence of the integer Courant number is restricted to the exponential term of equation (19), so M affects the phase but not the amplitude of the Fourier components.

In typical discrete Fourier series analysis the limit to the smallest wavelength that can be propagated is $2\Delta x$. However, methods which use the cubic Hermite basis can propagate waves to a limit of Δx.[14] This is due to the continuity of the first derivative at the nodes, and the reader is referred to Reference 15 for a discussion of sampling both the value and derivative of a signal. Accordingly, amplification factors can be computed for waves as small as Δx.

Since equation (18) is quadratic, $\tilde{\lambda}$ has two roots. One of them is the 'physical' root and mainly determines how ELLESCO propagates the solution. The second root is a 'computational' root and little affects the solution propagation. However, it can affect the stability of the numerial algorithm.

STABILITY

After n time steps the amplitude of a numerically propagated Fourier mode is $|F_m||\tilde{\lambda}_m|^n$ and, in principle, n can grow without bound. It follows that for a numerical algorithm to remain stable, $|\tilde{\lambda}_m| \leqslant 1$. As was mentioned earlier, two roots arise from equation (18), a 'physical' and a 'computational' root. Obviously, the amplitude of the physical root must remain less than one. Because computational modes can be introduced through round-off errors, the amplitude of the computational root must also remain less than one. Otherwise, the round-off errors will grow without bound.

Two cases arise depending on whether D is zero or not. When $D = 0$ there is no Θ dependence and the two roots become functions of *Co* and *ncel*. Figure 3 presents equal-amplitude contours as a function of Courant number and dimensionless wavelength for the case of *ncel* = 3. The

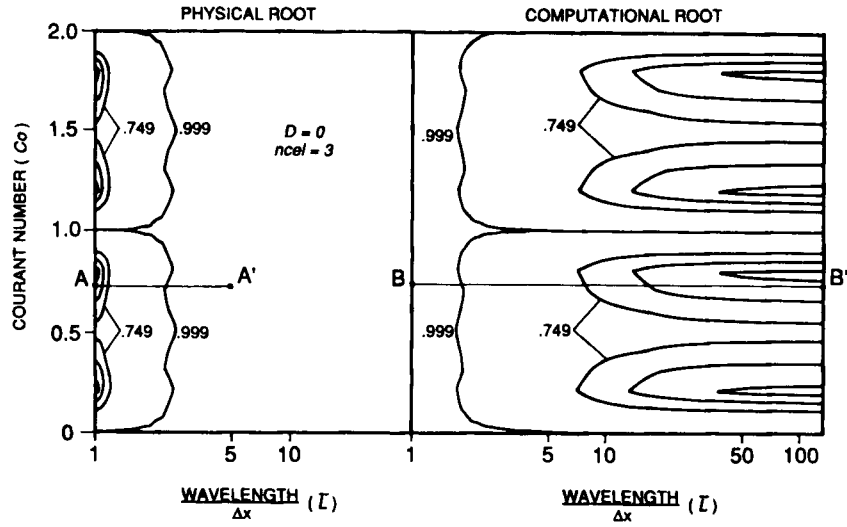

Figure 3. Contours of equal amplitude of the amplification factors. The amplitudes of the physical and computational amplification factors are contoured in the normalized wavelength–Courant number plane at 0·25 interval for $D = 0$, $ncel = 3$. The identical patterns for different values of M and the symmetry about $\alpha = 0{\cdot}5$ are characteristics of ELLESCO observed for any values of the problem parameters. The values do not exceed 1·0, demonstrating stability. See Figure 4 for profiles A–A′ and B–B′

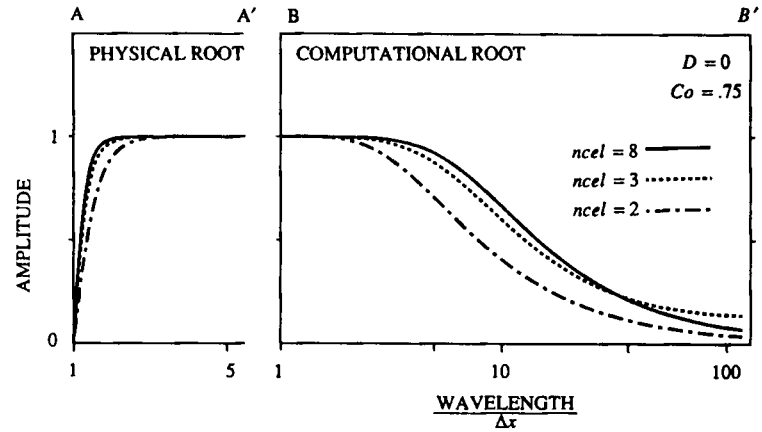

Figure 4. Amplification factor amplitudes versus normalized wavelength. Amplitude profiles for the physical (A–A′, Figure 3) and computational (B–B′, Figure 3) amplification factors are plotted for $D = 0$, $Co = 0{\cdot}75$ and $ncel = 2, 3, 8$. Both roots exhibit stability, and the longer wavelengths of the computational root are well damped

contour patterns repeat with changing integer Courant number, demonstrating that the amplitude has no dependence on M. Within each integer Courant number pattern the amplitude is also symmetric about $\alpha = 0{\cdot}5$. The form of the amplitude patterns exists regardless of the problem parameters.

Cross-sections along $Co = 0{\cdot}75$ for $ncel = 2$, 3 and 8 are shown in Figure 4. The analytic amplification factor amplitude is exactly one for all frequencies when D is zero. The physical root

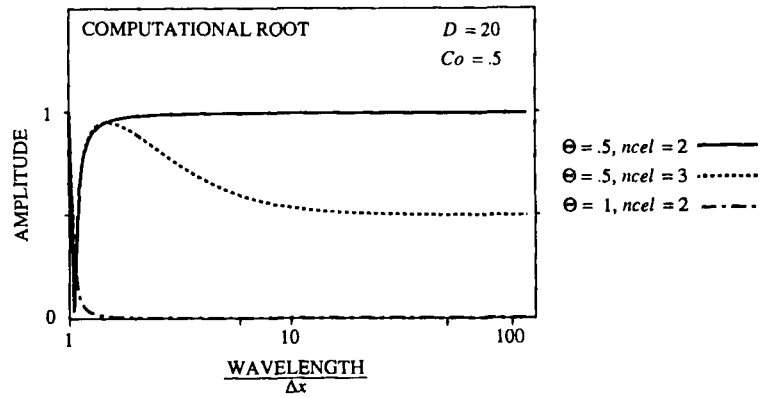

Figure 5. Computational root amplitude versus normalized wavelength. Amplitude profiles of the computational root are plotted for $D = 20$, $Co = 0{\cdot}5$ and ($\Theta = 0{\cdot}5$, $ncel = 2, 3$), ($\Theta = 1$, $ncel = 2$). The computational root is poorly damped when the Crank–Nicolson formulation is used with only two collocation points per element. The computational root is well damped by the implicit formulation except at $L = \Delta x$ where the computational root always has an amplitude of one

amplification factor amplitude is one for all but the shortest wavelengths, where it decreases rapidly. The computational root's amplitude is less than one for most wavelengths and is equal to one for only the shortest wavelengths. Both roots are stable for all *ncel*. For integer values of the Courant number ($\alpha = 0$) the two numerical amplification factors are equal and have an amplitude of one. When $ncel = 2$ there is an additional line of neutral stability at $\alpha = 0{\cdot}5$.

When D is not zero the amplification factor amplitudes also depend on the values of D and Θ. Many permutations of the problem parameters exist, so we summarize the basic stability results. Predictably, the implicit formulation ($\Theta = 1$) demonstrates the greatest stability, and all combinations of D, Co and *ncel* are stable. Similarly, the expected conditional stability was observed when $\Theta < 0{\cdot}5$. In all cases the computational root is equal to one when $L = \Delta x$. Thus there is no mechanism for attenuating Δx waves that are introduced into the computational mode through round-off error or poor initial conditions.

However, for the Crank–Nicolson scheme ($\Theta = 0{\cdot}5$) the computational root exhibits interesting behaviour (Figure 5). When the number of collocation points per element is greater than two the computational root is damped for all wavelengths greater than Δx. However, when $ncel = 2$ the computational root is only neutrally stable for long wavelengths. This result leads us to recommend the use of at least three collocation points per element with the Crank–Nicolson formulation.

ACCURACY

The computational roots are generally damped. Accordingly, the physical roots of the amplification factor mainly determine the accuracy of the numerical solution. In the discussion that follows we consider only the physical roots.

Let N'_m be the number of time steps required for the analytic solution to propagate the mth mode one wavelength:

$$N'_m = \frac{L_m}{V\Delta t} = \frac{\bar{L}_m}{Co}, \tag{20}$$

where $\bar{L}_m = L/\Delta x$ is the normalized wavelength.

A common measure of numerical performance is the amplitude ratio

$$R_m = \left(\frac{|\tilde{\lambda}_m|}{|\lambda_m|}\right)^{N'_m} = \left(\frac{|\tilde{\lambda}_m|}{\exp(-D\sigma_m^2 \Delta t)}\right)^{N'_m} = \left(\frac{|\tilde{\lambda}_m|}{\exp(-D\bar{\sigma}_m^2)}\right)^{N'_m}. \tag{21}$$

R_m is a measure of the amplitude error of the mth component of the numerical solution after the analytic wave has propagated one wavelength. When $R_m > 1$ the numerical solution has been insufficiently damped and when $R_m < 1$ it has been overdamped.

After N'_m time steps the phase of $\lambda_m^{N'_m}$ is, by the definition of N'_m, equal to 2π. A measure of the propagation error is the phase lag of the numeric solution after one complete wavelength has been travelled by the analytic mode:[1]

$$\Omega_m = N'_m \tan^{-1}\left(\frac{\operatorname{Im} \tilde{\lambda}_m}{\operatorname{Re} \tilde{\lambda}_m}\right) - 2\pi. \tag{22}$$

When $\Omega_m > 0$ the numeric mode is being propagated too rapidly and when $\Omega_m < 0$ it is being propagated too slowly.

The amplitude ratios and phase lags for $D = 0$, $ncel = 3$ and a variety of Courant numbers are plotted in Figure 6. The spectral behaviour of the numerical amplification factor tends to improve as the Courant number increases. In general, this is true for all ELMs and it has been noted previously.[11] The error per time step is not strongly dependent on the Courant number. However, solutions using larger Courant numbers require less time steps than those using smaller Courant numbers to advect a plume the same distance. Hence less error is accumulated per distance travelled.

Fourier modes with wavelengths greater than $2\Delta x$ are accurately propagated by ELLESCO when $D = 0$. Fourier analyses of other ELMs[2,6,11] indicate that accurate propagation by these

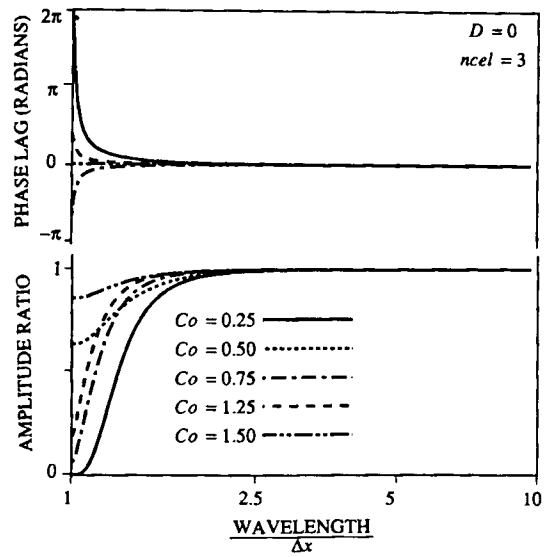

Figure 6. Amplitude ratio and phase lag versus normalized wavelength. Amplitude ratios and phase lags of the physical amplification factors are plotted for $D = 0$, $ncel = 3$ and $Co = 0{\cdot}25, 0{\cdot}50, 0{\cdot}75, 1{\cdot}25, 1{\cdot}50$. Note the lack of phase error when $Co = 0{\cdot}50$ and $1{\cdot}50$. In general, the spectral characteristics of the amplification factors of the zero-dispersion case improve as the Courant number and time step increase

methods does not occur until wavelengths are greater than $5\Delta x$. Accurate propagation does not occur for classical methods until the wavelength is significantly greater than $10\Delta x$.[1]

When dispersion is present the spatial discretization of a problem can be characterized by the Peclet number ($Pe = Co/D$). The velocity and dispersion coefficient are fixed by the physical setting of the problem and the spatial resolution is determined by the grid spacing. For a given spatial resolution the free parameter in the numerical method is the time step interval Δt. By fixing Pe and varying Co and D appropriately, we can see the effect of increasing the time step.

Figure 7 presents the amplitude ratio and phase lag results for $Pe = 10$, $ncel = 3$, $\Theta = 1$ and $D = 0{\cdot}025$, $0{\cdot}125$, $0{\cdot}925$ ($Co = 0{\cdot}25$, $1{\cdot}25$, $9{\cdot}25$). Increasing values of D and Co correspond to increasing Δt. As Δt increases, the numerical solution becomes increasingly underdamped. The two curves at the lower right of Figure 7 show the amplitude decay per time step of the analytic and numeric solutions for $D = 0{\cdot}925$. Although wavelengths less than $10\Delta x$ are underdamped, they are in phase. Narrow plumes will be propagated to the proper location, but they will be too narrow (Figure 8). This is opposite to the behaviour of the implicit formulation of classical methods, which tend to become too dispersed as Δt grows. However, Ewing and Russel[3] have observed similar behaviour in the single-step MMOC.

The dispersion number D is the parameter of importance when evaluating the effects of increasing Δt. Even in the presence of sharp fronts, implicit ELLESCO solutions will yield accurate solutions for $D \leqslant 0{\cdot}05$. For a given spatial discretization this is a limit on the time step. However, as time advances, the diffusive nature of the system will eliminate the higher spatial frequencies which are underdamped, and coarser discretizations can be implemented.

The Crank–Nicolson formulation ($\Theta = 0{\cdot}5$) of ELLESCO behaves quite differently from the implicit formulation. Figure 9 presents the amplitude ratios and phase lags for $\Theta = 0{\cdot}5$, $ncel = 3$,

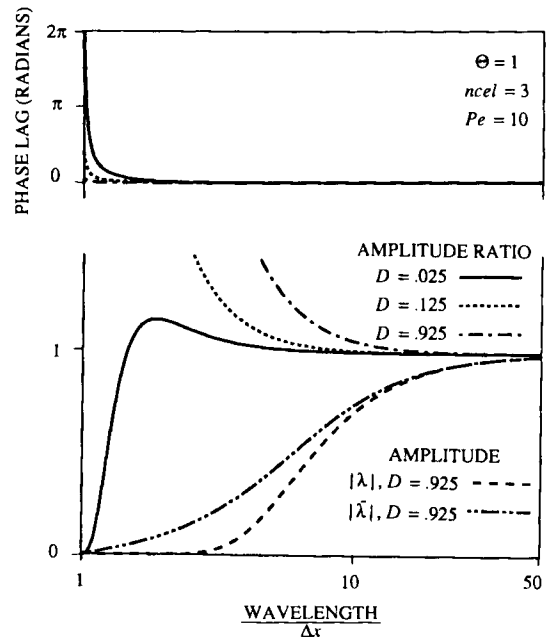

Figure 7. Amplitude ratio and phase lag versus normalized wavelength. Amplitude ratios and phase lags of the physical amplification factors are plotted for $\Theta = 1$, $ncel = 3$, $Pe = 10$ and $D = 0{\cdot}025$, $0{\cdot}125$, $0{\cdot}925$ ($Co = 0{\cdot}25$, $1{\cdot}25$, $9{\cdot}25$). In addition, the two lower right curves are the amplitudes of the numeric and analytic amplification factors for $D = 0{\cdot}925$. As D increases, solutions become increasingly underdamped. Phase errors decrease with increasing D.

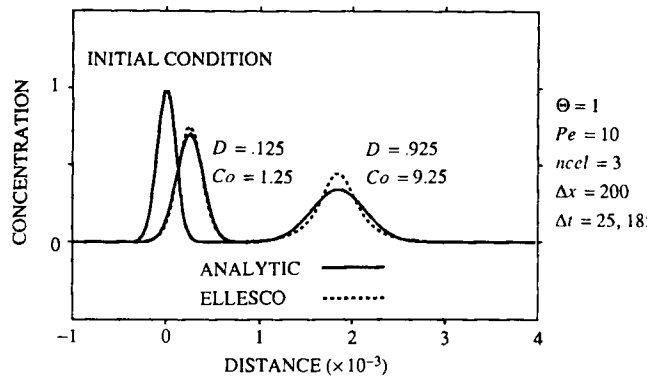

Figure 8. Propagation of a Gaussian plume by implicit ELLESCO. A Gaussian plume with standard deviation of 99 is propagated one time step by ELLESCO using $\Theta = 1$, $Pe = 10$, $\Delta x = 200$, $D = 0{\cdot}125$, $0{\cdot}925$ and $\Delta t = 25$, 185. Solid lines are initial conditions and analytic solutions. Broken lines are ELLESCO-computed solutions. The underdamping predicted in Figure 7 leads to solutions which are too steep and tall

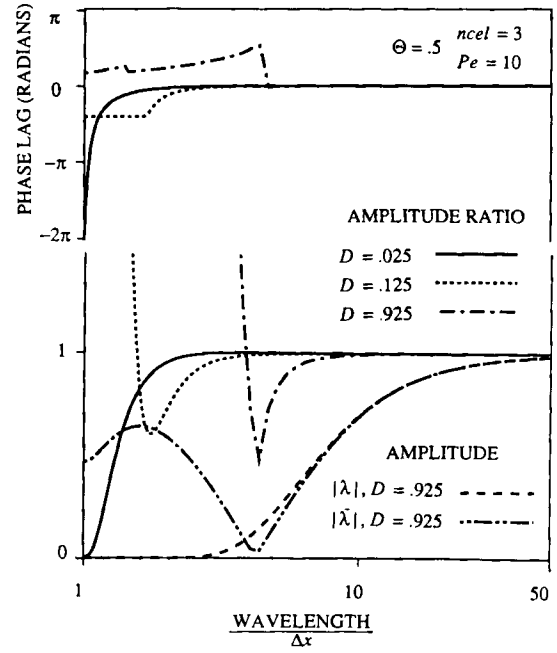

Figure 9. Amplitude ratio and phase lag versus normalized wavelength. Amplitude ratios and phase lags of the physical amplification factors are plotted for $\Theta = 0{\cdot}5$, $ncel = 3$, $Pe = 10$ and $D = 0{\cdot}025$, $0{\cdot}125$, $0{\cdot}925$ ($Co = 0{\cdot}25$, $1{\cdot}25$, $9{\cdot}25$). In addition, the two lower right curves are plots of the amplitudes of the numeric and analytic amplification factors for $D = 0{\cdot}925$. As D increases, a discontinuity develops in the character of the amplification factor. Short wavelengths become underdamped and badly out of phase

$Pe = 10$ and $D = 0{\cdot}025$, $0{\cdot}125$, $0{\cdot}925$. When $D = 0{\cdot}025$, wavelengths of $2\Delta x$ and longer are propagated quite accurately. Shorter wavelengths are lagged and overdamped. This leads to excellent solutions in the presence of sharp features.

As Δt (and therefore D) is increased, the overdamping begins at longer wavelengths, but the phase remains accurate until a discontinuity in the behaviour of the numerical amplification

factor occurs in the shorter wavelengths. This abrupt change in behaviour occurs at about $2\Delta x$ for $D = 0{\cdot}125$ and $4\Delta x$ for $D = 0{\cdot}925$. At these wavelengths an abrupt change in phase occurs and the smaller wavelengths becomes severely underdamped. The two curves at the lower right of Figure 9 show the amplitudes of the analytic and numeric amplification factors when $D = 0{\cdot}925$.

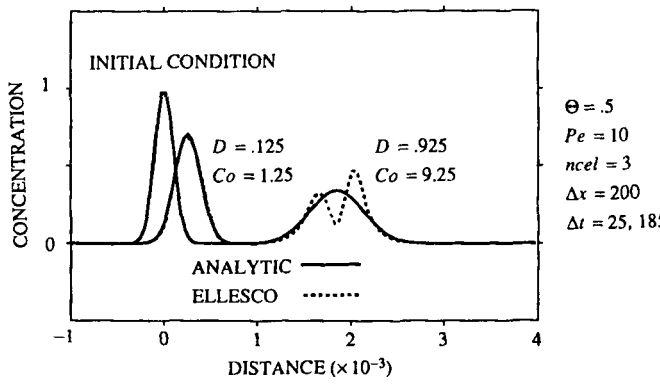

Figure 10. Propagation of a Gaussian plume by Crank–Nicolson ELLESCO. A Gaussian plume with standard deviation of 99 is propagated one time step by ELLESCO using $\Theta = 0{\cdot}5$, $Pe = 10$, $\Delta x = 200$, $D = 0{\cdot}125$, $0{\cdot}925$ and $\Delta t = 25$, 185. Solid lines are initial conditions and analytic solutions. Broken lines are ELLESCO-computed solutions. When D gets large, the phase errors and underdamping shown in Figure 9 lead to oscillations. Note the improvement over the implicit solution for $D = 0{\cdot}125$

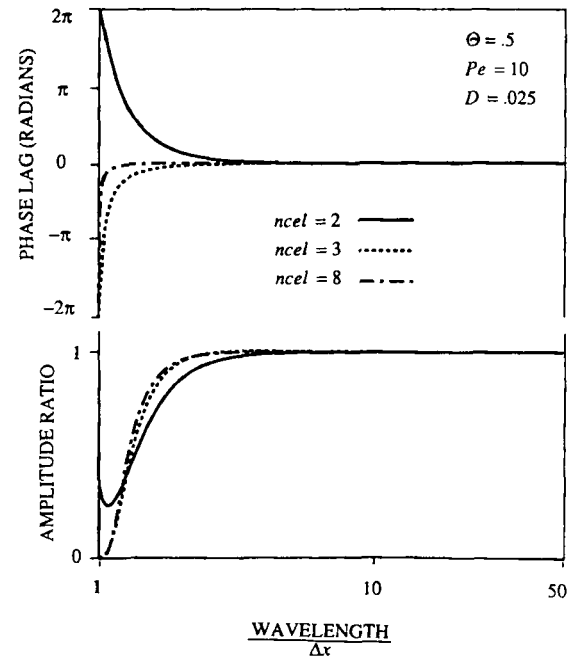

Figure 11. Amplitude ratio and phase lag versus normalized wavelength. The amplitude ratio and phase lag are plotted for $\Theta = 0{\cdot}5$, $Pe = 10$, $D = 0{\cdot}025$ and $ncel = 2, 3, 8$. As the number of collocation points per element increases, the spectral behaviour of the physical amplification factor improves. The greatest improvement occurs as $ncel$ increases from two to three

The wavelengths around $2\Delta x$ are significantly underdamped and badly out of phase. Even more disturbing, these modes will decay slowly because the amplitude of the numeric amplification factor is relatively large ($|\tilde{\lambda}| \approx 0{\cdot}6$). The effects of the phase and amplitude errors are illustrated in Figure 10. Good results are obtained for $D \leqslant 0{\cdot}125$ and, as time increases and the shorter wavelengths are damped, coarser discretizations can be used.

The oscillatory behaviour at large Δt is equivalent to the well understood oscillatory behaviour of finite difference solutions to the heat flow equation.[16] Groundwater flow modellers have also seen this behaviour when taking too large an initial time step in the presence of discontinuous initial conditions. In other words, the oscillations are not a result of the Eulerian–Lagrangian procedure; rather, they are the result of taking too large a time step when solving the parabolic problem with an elliptic spatial operator.

The number of collocation points per element also affects the amplification factors of the ELLESCO method. Figure 11 presents the amplitude ratio and phase lag results for $\Theta = 0{\cdot}5$, $Pe = 10$, $D = 0{\cdot}025$ and $ncel = 2, 3, 8$. As the number of collocation points increases, both the amplitude and phase behaviour improve. Most of the improvement in accuracy is gained by going from two to three collocation points. Since increasing the number of collocation points also increases the computational burden, three collocation points per element in one-dimensional problems and nine collocation points per element in two-dimensional problems is the recommended base pattern when short spatial wavelengths exist in the concentration field. This is consistent with the analysis of test problem results.

CONCLUSIONS

A Fourier analysis of the ELLESCO method has been performed. The amplification factors that characterize the solution were derived by treating each degree of freedom associated with the nodes as an independent variable and expanding them in separate Fourier series. A homogeneous matrix equation was derived, and the required singularity of the system matrix was used to derive a quadratic equation for the amplification factor. This approach can be used for the Fourier analysis of any system of mixed node types or multiple degrees of freedom per node.

Stability for all $\Theta \geqslant 0{\cdot}5$ has been demonstrated. However, the computational root is only neutrally stable at long wavelengths when $\Theta = 0{\cdot}5$ and $ncel = 2$.

The main advantages of ELLESCO are found when solving problems of advection-dominated transport. The removal of the first-order term will not reduce the discretization limits arising from the numerical solution of the transient diffusion problem. For the pure advection case, excellent phase and amplitude behaviour are observed. Larger time steps will improve the solution and, in parctice, the complexities of the velocity field will determine the ultimate limit of Δt.

As dispersion becomes important, the time step associated with a given spatial accuracy becomes limited, and the dimensionless parameter which characterizes the limit is the dispersion number. If short spatial wavelengths are present with significant amplitude, dispersion numbers for the implicit case should be kept to less than 0·05 or the solution will be underdamped. For the $\Theta = 0{\cdot}5$, case, D should be kept to less than 0·125 or phase and amplitude errors can begin to cause oscillations. In the case of very large dispersion numbers, these artefacts will persist for many time steps. As the shorter wavelengths are attenuated by dispersion, the discretization can be relaxed by either increasing Δt and D or by increasing both Δt and Δx and keeping D constant.

Finally, Fourier analysis results demonstrate that more collocation points per element improves the spectral behaviour of the amplification factor. Most of the improvement is gained by going from two to three points per element.

ACKNOWLEDGEMENT

We wish to acknowledge support from the Air Force Office of Scientific Research, Bolling AFB, DC.

APPENDIX I

The coefficients of equation (8) obtained for the geometry of Figure 1 are presented in this appendix. In the example there are three collocation points per element, *ncel* = 3, and six collocation points contribute to the final coefficients. Although the summation details will vary with *ncel* and α, the general form of the equations will not change, and the interested reader can use this appendix as a guide when deriving the coefficients for other configurations.

Define the operators

$$L_1 \equiv \left(1 - 4\Theta D \frac{\partial^2}{\partial \xi^2}\right),$$

$$L_2 \equiv \left(1 + 4(1-\Theta) D \frac{\partial^2}{\partial \xi^2}\right). \tag{23}$$

The coefficients associated with the unknown values of C_q^{n+1} and CX_q^{n+1} are the terms found in the system matrix of the ELLESCO algebraic system of equations. They are computed as

$$a_1^0 = \sum_{k=1}^{3} L_1\Phi_0^0(\xi_k) L_1\Phi_1^0(\xi_k),$$

$$a_2^0 = \sum_{k=1}^{3} L_1\Phi_0^1(\xi_k) L_1\Phi_1^0(\xi_k),$$

$$a_3^0 = \sum_{k=1}^{3} [L_1\Phi_1^0(\xi_k) L_1\Phi_1^0(\xi_k) + L_1\Phi_0^0(\xi_k) L_1\Phi_0^0(\xi_k)],$$

$$a_4^0 = \sum_{k=1}^{3} [L_1\Phi_1^1(\xi_k) L_1\Phi_1^0(\xi_k) + L_1\Phi_0^1(\xi_k) L_1\Phi_0^0(\xi_k)],$$

$$a_5^0 = \sum_{k=1}^{3} L_1\Phi_1^0(\xi_k) L_1\Phi_0^0(\xi_k),$$

$$a_6^0 = \sum_{k=1}^{3} L_1\Phi_1^1(\xi_k) L_1\Phi_0^0(\xi_k). \tag{24}$$

Coefficients a_1^1 to a_6^1 are computed using the weighting function of equation (6b). Their form will be the same as the equivalent terms in the above equations except that the right-hand factors of the products are replaced with the Φ_j^1 equivalents. For example,

$$a_3^1 = \sum_{k=1}^{3} [L_1\Phi_1^0(\xi_k) L_1\Phi_1^1(\xi_k) + L_1\Phi_0^0(\xi_k) L_1\Phi_0^1(\xi_k)]. \tag{25}$$

The coefficients associated with the terms from the previous time level, C_q^n and CX_q^n, are contained in the right-hand-side vector of the ELLESCO matrix equations. They are computed as

$$f_1^0 = L_2\Phi_0^0(\xi_1 - 2\alpha + 2) L_1\Phi_1^0(\xi_1),$$

$$f_2^0 = L_2\Phi_0^1(\xi_1 - 2\alpha + 2) L_1\Phi_1^0(\xi_1),$$

$$f_3^0 = L_2\Phi_1^0(\xi_1 - 2\alpha + 2)L_1\Phi_1^0(\xi_1) + \sum_{k=2}^{3} L_2\Phi_0^0(\xi_k - 2\alpha)L_1\Phi_1^0(\xi_k) + L_2\Phi_0^0(\xi_1 - 2\alpha + 2)L_1\Phi_0^0(\xi_1),$$

$$f_4^0 = L_2\Phi_1^1(\xi_1 - 2\alpha + 2)L_1\Phi_1^0(\xi_1) + \sum_{k=2}^{3} L_2\Phi_0^1(\xi_k - 2\alpha)L_1\Phi_1^0(\xi_k) + L_2\Phi_0^1(\xi_1 - 2\alpha + 2)L_1\Phi_0^0(\xi_1),$$

$$f_5^0 = \sum_{k=2}^{3} L_2\Phi_1^0(\xi_k - 2\alpha)L_1\Phi_1^0(\xi_k) + L_2\Phi_1^0(\xi_1 - 2\alpha + 2)L_1\Phi_0^0(\xi_1) + \sum_{k=2}^{3} L_2\Phi_0^0(\xi_k - 2\alpha)L_1\Phi_0^0(\xi_k),$$

$$f_6^0 = \sum_{k=2}^{3} L_2\Phi_1^1(\xi_k - 2\alpha)L_1\Phi_1^0(\xi_k) + L_2\Phi_1^1(\xi_1 - 2\alpha + 2)L_1\Phi_0^0(\xi_1) + \sum_{k=2}^{3} L_2\Phi_0^1(\xi_k - 2\alpha)L_1\Phi_0^0(\xi_k),$$

$$f_7^0 = \sum_{k=2}^{3} L_2\Phi_1^0(\xi_k - 2\alpha)L_1\Phi_0^0(\xi_k),$$

$$f_8^0 = \sum_{k=2}^{3} L_2\Phi_1^1(\xi_k - 2\alpha)L_1\Phi_0^0(\xi_k). \tag{26}$$

Coefficients f_1^1 to f_8^1 are computed as above, but the right-hand factors of the products are replaced with the Φ_j^1 equivalents. For example,

$$f_5^1 = \sum_{k=2}^{3} L_2\Phi_1^0(\xi_k - 2\alpha)L_1\Phi_1^1(\xi_k) + L_2\Phi_1^0(\xi_1 - 2\alpha + 2)L_1\Phi_0^1(\xi_1) + \sum_{k=2}^{3} L_2\Phi_0^0(\xi_k - 2\alpha)L_1\Phi_0^1(\xi_k). \tag{27}$$

The co-ordinates ξ_k are uniquely specified by the number of collocation points per element, *ncel*. Hence the a and f coefficients are functions of the dimensionless dispersion number, the time weight and the number of collocation points per element. The f coefficients are also dependent on the fractional Courant number. The definitions of Φ_0^1 and Φ_1^1 contain Δx, but this dependence will vanish in the derivation of the amplification factor and is of no significance.

APPENDIX II

This appendix contains some details from the development of equation (19). We define the following groupings:

$$A_O^0 \equiv a_1^0 e^{-i\sigma} + a_3^0 + a_5^0 e^{i\sigma},$$

$$A_E^0 \equiv a_2^0 e^{-i\sigma} + a_4^0 + a_6^0 e^{i\sigma},$$

$$A_O^1 \equiv a_1^1 e^{-i\sigma} + a_3^1 + a_5^1 e^{i\sigma},$$

$$A_E^1 \equiv a_2^1 e^{-i\sigma} + a_4^1 + a_6^1 e^{i\sigma},$$

$$F_O^0 \equiv f_1^0 e^{-i2\sigma} + f_3^0 e^{-i\sigma} + f_5^0 + f_7^0 e^{i\sigma},$$

$$F_{\mathrm{E}}^{0} \equiv f_2^0 e^{-i2\sigma} + f_4^0 e^{-i\sigma} + f_6^0 + f_8^0 e^{i\sigma},$$
$$F_{\mathrm{O}}^{1} \equiv f_1^1 e^{-i2\sigma} + f_3^1 e^{-i\sigma} + f_5^1 + f_7^1 e^{i\sigma},$$
$$F_{\mathrm{E}}^{1} \equiv f_2^1 e^{-i2\sigma} + f_4^1 e^{-i\sigma} + f_6^1 + f_8^1 e^{i\sigma}. \tag{28}$$

The matrix elements of equation (17) become

$$\mu_{11} = A_{\mathrm{O}}^{0}\tilde{\lambda} - F_{\mathrm{O}}^{0} e^{-i\sigma M},$$
$$\mu_{12} = A_{\mathrm{E}}^{0}\tilde{\lambda} - F_{\mathrm{E}}^{0} e^{-i\sigma M},$$
$$\mu_{21} = A_{\mathrm{O}}^{1}\tilde{\lambda} - F_{\mathrm{O}}^{1} e^{-i\sigma M},$$
$$\mu_{22} = A_{\mathrm{E}}^{1}\tilde{\lambda} - F_{\mathrm{E}}^{1} e^{-i\sigma M}. \tag{29}$$

Substituting the above relations into equation (18) we arrive at the expanded form

$$(A_{\mathrm{O}}^{0}A_{\mathrm{E}}^{1} - A_{\mathrm{O}}^{1}A_{\mathrm{E}}^{0})\tilde{\lambda}^2 + e^{-i\sigma M}(-A_{\mathrm{O}}^{0}F_{\mathrm{E}}^{1} - A_{\mathrm{E}}^{1}F_{\mathrm{O}}^{0} + A_{\mathrm{O}}^{1}F_{\mathrm{E}}^{0} + A_{\mathrm{E}}^{0}F_{\mathrm{O}}^{1})\tilde{\lambda}$$
$$+ e^{-i2\sigma M}(F_{\mathrm{O}}^{0}F_{\mathrm{E}}^{1} - F_{\mathrm{O}}^{1}F_{\mathrm{E}}^{0}) = 0. \tag{30}$$

At this point we note that all of the terms with subscript E contain a Δx residing in the definition of the Φ_j^1 basis functions. Similarly, those terms with superscript 1 contain a Δx due to the Φ_j^1 basis functions in the weighting function. Dividing through by Δx^2 eliminates all Δx dependence outside of the dimensionless variables.

The equation (19) parameters are

$$\bar{a} = A_{\mathrm{O}}^{0}A_{\mathrm{E}}^{1} - A_{\mathrm{O}}^{1}A_{\mathrm{E}}^{0},$$
$$\bar{b} = -A_{\mathrm{O}}^{0}F_{\mathrm{E}}^{1} - A_{\mathrm{E}}^{1}F_{\mathrm{O}}^{0} + A_{\mathrm{O}}^{1}F_{\mathrm{E}}^{0} + A_{\mathrm{E}}^{0}F_{\mathrm{O}}^{1},$$
$$\bar{c} = F_{\mathrm{O}}^{0}F_{\mathrm{E}}^{1} - F_{\mathrm{O}}^{1}F_{\mathrm{E}}^{0}. \tag{31}$$

The least squares method produces a symmetric system matrix which leads to the following identities (see Appendix I):

$$a_1^0 = a_5^0,$$
$$a_2^1 = a_6^1,$$
$$a_4^0 = a_3^1,$$
$$a_6^0 = a_1^1. \tag{32}$$

In addition, the asymmetry of the Φ_j^1 basis functions combined with the symmetric placement of the collocation points leads to

$$a_2^0 = -a_6^0,$$
$$a_5^1 = -a_1^1. \tag{33}$$

By applying the equalities of equations (32) and (33) to the definitions of A in equation (28), it can be shown that A_{O}^0 and A_{E}^1 are real and that A_{E}^0 and A_{O}^1 are complex conjugates. We conclude that $\bar{a}$ is a real function of D, Θ, *ncel* and $\bar{\sigma}$. In general, $\bar{b}$ and $\bar{c}$ are complex functions of D, Θ, *ncel*, $\bar{\sigma}$ and α.

An interesting exception is for wavelength $L = 2\Delta x$. For this particular case $\bar{\sigma} = \pi$ and $\bar{a}$, $\bar{b}$, $\bar{c}$ and the exponential term in equation (19) are all real. However, if $4\overline{ac}$ is greater than $\bar{b}^2$, which is the case for small to moderate values of D, the two roots of the amplification factor will have the same amplitude and opposite phase.

REFERENCES

1. G. F. Pinder and W. G. Gray, *Finite Element Simulation in Surface and Subsurface Hydrology*, Academic Press, New York, 1977.
2. F. M. Holly Jr. and A. Preissmann, 'Accurate calculation of transport in two dimensions', *J. Hydrol. Div. ASCE*, **HY11**, 1259–1277 (1977).
3. R. E. Ewing and T. F. Russel, 'Multistep Galerkin methods along characteristics for convection–diffusion problems', in *Advances in Computer Methods for Partial Differential Equations, IV*, R. Vichnevetsky and R. S. Stepleman (eds), IMACS, Rutgers University, New Brunswick, New Jersey, 1981, pp. 28–36.
4. S. P. Neuman, 'A Eulerian–Lagrangian numerical scheme for the dispersion–convection equation using conjugate space–time grids', *J. Comput. Phys.*, **41**, 270–294 (1981).
5. J. Douglas Jr. and T. F. Russel, 'Numerical methods for convection-dominated diffusion problems based on combining the method of characteristics with finite element or finite difference procedures', *SIAM J. Numer. Anal.*, **19**, 871–885 (1982).
6. J. Glass and W. Rodi, 'A higher order numerical scheme for scalar transport', *Comput. Methods Appl. Mech. Eng.*, **31**, 337–358 (1982).
7. S. P. Neuman and S. Sorek, 'Eulerian–Lagrangian methods for advection–dispersion', in K. P. Mole *et al.* (eds), *Finite Elements in Water Resources, Vol. 4*, 1982, pp. 14.41–14.68.
8. F. M. Holly Jr. and T. Komatsu, 'Derivative approximations in the two-point fourth order method for pollutant transport', *Proc. Conf. on Frontiers in Hyderol. Engineering*, ASCE, MIT, Cambridge, MA, 1983, pp. 349–355.
9. A. E. Baptista, E. E. Adams and K. D. Stolzenbach, 'Eulerian–Lagrangian analysis of pollutant transport in shallow water', *Ralph M. Parsons Laboratory, MIT, Report No. 296*, 1984.
10. T. Komatsu, F. M. Holly Jr., N. Nakashiki and K. Ohgushi, 'Numerical calculation of pollutant transport in one and two dimensions', *J. Hydrosci. Hydrol. Eng.*, **3**, 15–30 (1985).
11. A. E. Baptista, 'Solution of advection-dominated transport by Eulerian–Lagrangian methods using the backwards method of characteristics', *Ph.D. Dissertation*, MIT, Cambridge, MA, 1987.
12. K. Toda and F. M. Holly, 'Hybrid numerical method for linear advection–diffusion', *Microsoftware Eng.*, **3**, 199–205 (1987).
13. L. R. Bentley, G. F. Pinder and I. Herrera, 'Solution of the advective–dispersive transport equation using a least squares collocation, Eulerian–Lagrangian method', *Numer. Methods PDE*, **5**, 227–240 (1989).
14. A. Shapiro and G. F. Pinder, 'Analysis of an upstream weighted collocation approximation to the transport equation', *J. Comput. Phys.*, **39**, 46–71 (1981).
15. R. Bracewell, *The Fourier Transform and its Applications*, McGraw-Hill, New York, 1965.
16. S. H. Crandall, 'An optimum implicit recurrence formula for the heat conduction equation', *Quart. Appl. Math.*, **13**, 318–320 (1955).